Plasma photonic spatiotemporal synchronization of relativistic electron and laser beams

P. Scherkl[1,2,3] A. Knetsch[14] T. Heinemann[1,2,4] A. Sutherland,[1,2,6] A. F. Habib,[1,2]
O. S. Karger,[5] D. Ullmann,[1,2,13] A. Beaton,[1,2] G. G. Manahan,[1,2] Y. Xi,[7] A. Deng,[7] M. D. Litos,[8]
B. D. O'Shea,[6] S. Z. Green[6] C. I. Clarke,[6] G. Andonian[7,9] R. Assmann,[4] D. L. Bruhwiler[10]
J. Smith,[11] J. R. Cary,[8,12] M. J. Hogan,[6] V. Yakimenko,[6] J. B. Rosenzweig,[7] and B. Hidding[1,2]

[1]*SUPA, Department of Physics, University of Strathclyde, Glasgow G1 1XQ, United Kingdom*
[2]*The Cockcroft Institute, Daresbury, Warrington WA4 4AD, United Kingdom*
[3]*Business Division of Safety, Security, and Compliance, University Medical Center Hamburg-Eppendorf, 20246 Hamburg, Germany*
[4]*Deutsches Elektronen-Synchrotron DESY, Notkestrasse 85, 22607 Hamburg, Germany*
[5]*Department of Experimental Physics, University of Hamburg, 20355 Hamburg, Germany*
[6]*SLAC National Accelerator Laboratory, Menlo Park, California 94025, USA*
[7]*Department of Physics and Astronomy, University of California, Los Angeles, California 90095-1547, USA*
[8]*Center for Integrated Plasma Studies, Department of Physics, University of Colorado, Boulder, Colorado 80309-0390, USA*
[9]*Radiabeam Technologies, Santa Monica, California 90404, USA*
[10]*RadiaSoft LLC, Boulder, Colorado 80301, USA*
[11]*Tech-X UK Limited, Daresbury, Warrington WA4 4AD, United Kingdom*
[12]*Tech-X Corporation, Boulder, Colorado 80303, USA*
[13]*Faculty of Physics and Astronomy, Friedrich-Schiller-Universität Jena, 07743 Jena, Germany*
[14]*LOA, ENSTA Paris, CNRS, Ecole Polytechnique, Institut Polytechnique de Paris, 91762 Palaiseau, France*

We present an ultracompact plasma-based method to measure spatial and temporal concurrence of intense electron and laser beams nonintrusively at their interaction point. The electron beam couples with a laser-generated seed plasma in dependence of spatiotemporal overlap, which triggers additional plasma production and manifests as enhanced plasma afterglow. This optical observable is exploited to measure beam concurrence with ~ 4 μm spatial and ~ 26.7 fs temporal accuracy, supported by auxiliary diagnostics. The afterglow interaction fingerprint is highly sensitive and enables ultraversatile femtosecond-micrometer beam metrology.

Femtosecond-duration particle beams concomitant with similarly short laser pulses are increasingly important in exciting and probing ultrafast processes [1–3] occurring in plasma, molecular, atomic, and nuclear structures. For example, modern light sources such as free-electron lasers [4,5] and inverse Compton scattering [6–11] require precise spatiotemporal control of laser-electron beam interactions. An emerging class of plasma accelerators [12–17] also strongly benefits from the spatiotemporal coordination of electron and laser beams for driving plasma waves, injection processes, and (staged) acceleration of high-quality particle beams. This demand has given rise to a broad range of synchronization and alignment techniques, such as electro-optic sampling (EOS) [18,19], measurement techniques based on excited cavities [20], coherent transition radiation 21]], cross-correlated terahertz radiation from undulators [22], and various schemes in free-electron lasers [23]. These techniques individually offer either measurement of temporal synchronization or spatial alignment of electron and laser beams. To measure both, combinations of diagnostics must be implemented separately along the beam line. Furthermore, damage thresholds prohibit intercepting diagnostics for more intense and focused laser and electron beams, such that they must be employed away from the beam focus and/or at reduced beam power levels at the interaction point (IP). The same reasons prevent their application in the presence of plasma.

In this paper, we address these demands and challenges and report on a versatile plasma photonic metrology technique, showcased for measuring spatial and temporal coordination of intense laser and electron beams directly at their IP. These capabilities arise from exploiting the interaction of an electron beam with a confined seed plasma filament generated by a focused laser pulse via tunneling ionization. The plasma eventually recombines, emitting afterglow radiation with characteristic spectral lines of the respective medium [24,25]. In contrast to scenarios where the laser pulse transfers significant energy to the plasma electrons via inverse bremsstrahlung, which can be exploited for laser guiding applications [26–28], the laser-generated seed plasma in our configuration is cold with a temperature of few eV. Those seed plasma electrons which couple with the unipolar electric field of the transiently overlapping electron beam, however, gain substantially higher kinetic energies. Over time, this energy converts to additional plasma, which can be detected as substantially amplified plasma afterglow yield. This coupling of spatio-temporal overlap between laser pulse and electron beam—with plasma as a conjunctive emitter medium—can be exploited to derive highly sensitive interaction fingerprints.

We conducted proof-of-concept experiments at the Facility for Advanced Accelerator Experimental Tests (FACET) [29] at the SLAC National Accelerator Laboratory. Here, the linac provides an ultrarelativistic electron beam of 20 GeV energy, a total charge of $Q_b \approx 3.0$ nC $\pm 0.6\%$, length of $\sigma_z \approx 64$ μm $\pm 1.9\%$, focused to a transverse size of $\sigma_x \approx 22$ μm and $\sigma_y \approx 44$ μm [all root-mean-square (rms)]. The corresponding peak electron density amounts to $n_{b0} = Q_b/(2\pi)^{3/2} e\sigma_x\sigma_y\sigma_z \approx 1.9 \times 10^{16}$ cm^{-3}. This beam traverses a mixed H_2/He gas reservoir with 1∶1 ratio at 5.3 mbar. It does not generate observable plasma, because its radial electric field $E_r(r) = [n_{b0}e/2^{3/2}\epsilon_0\sigma_z r][1 - \exp(-r^2/2\sigma_r^2)] \approx 3$ GV/m is below the tunneling ionization threshold for hydrogen. Here, r is the radial coordinate, e is the elementary charge, and ϵ_0 the vacuum permittivity. Likewise, impact ionization by the transient electron beam is negligible due to the low cross sections associated with highly relativistic electron energies [30,31]. The setup shown in Fig. 1 further employs a Ti: sapphire laser pulse with a duration of $\tau_L \approx 60$ fs full width at half maximum (FWHM). Several meters upstream of the electron beam focus, a collimated low-intensity split-off laser pulse is superimposed with the electric field of the unfocused electron beam on a 100-μm-thick gallium phosphide (GaP) crystal for EOS under 45°. It provides relative shot-to-shot time-of-arrival (TOA) measurements with an accuracy of $\tau_{EOS} = 25.8 \pm 2.5$ fs and quantifies the system-inherent TOA jitter of 109 ± 12 fs (rms). The EOS as established diagnostics benchmarks the plasma-based TOA measurements at the IP. The other laser arm is focused perpendicularly to a spot size of $w_0 \approx 38$ μm (FWHM) into the focal region of the electron beam and is afterward imaged
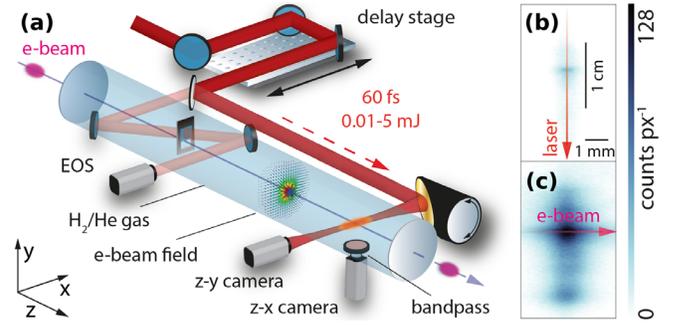
FIG. 1. Experimental setup and afterglow shots: (a) The electron beam propagates through gas and couples with an overlapping laser-generated seed plasma. (b) Example of laser-only plasma afterglow at 587 nm. (c) Example of electron-beam-enhanced plasma afterglow.

by a (z-y) CCD camera. Tuning the energy of this linearly y-polarized laser pulse up to 5 mJ yields intensities of $I_L \approx 10^{14}$–10^{15} W cm^{-2} in the gas, which generates a cold, centimeter-long H_2/He plasma filament of width $d_{plasma} \approx 100$ μm via tunneling ionization [32]. Full ionization of hydrogen and the first level of helium yields the effective plasma electron density $n_e \approx 1.9 \times 10^{17}$ cm$^{-3} \approx 10 \times n_{b0}$ such that the plasma is overdense with respect to the electron beam. Additionally, the electron beam duration is longer than the width of the seed plasma filament; both attributes ensure a quasiadiabatic and linear interaction. A second (z-x) CCD camera with a 10-nm-wide bandpass filter monitors the interaction region and integrates radiation from the characteristic He plasma afterglow line $\lambda_{He} \approx 584$ nm [33] over 25 ms in a solid angle of $\approx 4.6 \times 10^{-3}$ sr and detects an average integrated noise of ~707 counts per image. A motorized optical transition radiation screen at the IP marks the electron beam orbit and allows for initial coarse spatial overlap with the laser pulse at low power. The shot-to-shot pointing jitter of electron beam and laser pulse amounts to $\sigma_{e,y} \approx 6.6$ μm (rms) and $\sigma_{L,y} \approx 7.6$ μm (rms), respectively, resulting in combined shot-to-shot jitter of $(\sigma_{e,y}^2 + \sigma_{L,y}^2)^{1/2} \approx 10.1$ μm in the y direction. After these reference measurements, the OTR has to be removed to prevent damage caused by higher laser power. The laser pulse then generates the seed plasma filament as shown in Fig. 1(b). When the electron beam arrives at the IP after the laser pulse, it interacts with this thin plasma filament. This interaction distinctively amplifies the integrated afterglow signal as shown in Fig. 1(c), thereby increasing the detected photon signal ~42× from ~6.2 × 10⁴ counts to ~2.6 × 10⁶ counts and the radiating volume ~15×, which is attributed to generation of additional plasma via secondary ionization events and plasma expansion.

We explore the initial interaction between the electron beam and the laser-generated seed plasma filament by modeling the experimental situation in fully explicit 3D particle-in-cell (PIC) simulations using vsim [34]. The simulation box size is 1.9 mm × 1.6 mm × 0.8 mm with 3 μm cell size, filled with 16 macroparticles per cell for the
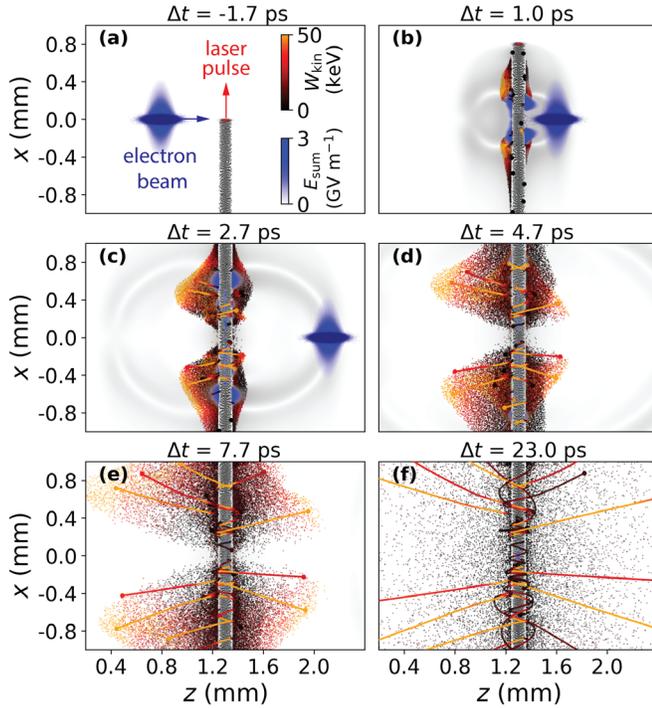
FIG. 2. PIC-simulation snapshots. (a) The electron beam approaches the emerging laser-generated H_2/He plasma filament (black dots), reaching the filament center at $\Delta t = 0$. (b),(c) The electron beam crosses the filament and heats plasma electrons via its unipolar transverse field (blue). Plasma surface waves (blue, central slice of simulation) propagate along the filament and transport density perturbations. (d)–(f) Localized plasma electron oscillations visualized by typical electron trajectories (solid lines), color coded by momentary energy.

bi-Gaussian electron beam and eight macroparticles per cell for each gas component. We model the laser pulse in the envelope approximation and generate the plasma filament by tunneling ionization of hydrogen and helium. Figure 2 presents simulation snapshots, where the electron beam briefly couples with the seed plasma filament for the duration of their geometrical overlap. Because of the linear interaction regime, the electron beam represents a perturbation to the filament, and ambient plasma electrons rapidly screen the strong electric field, as the skin depth $k_p^{-1} = (\epsilon_0 m_e c^2/n_e e^2)^{1/2} \approx 12~\mu m$, with m_e being the electron mass and c the speed of light. Consequently, significant energy transfer occurs only within the direct overlap volume. In this case, the electron beam deposits 0.93 mJ or $1.3 \times 10^{-3}\%$ of its ~ 67 J total kinetic energy during the short interaction with the plasma—a negligible energy loss for the electron beam but a significant energy gain of the seed plasma electrons. Those obtain broadband velocities with average energy $\bar{W}_{kin} \approx 400$ eV. A significant fraction further obtains peak energies $W_{max} \approx \pi(eE_{peak}\sigma_z/\beta c)^2/m_e \approx$ hundreds of keV and escapes from the initial filament volume. Here, E_{peak} denotes the peak radial electric field of the beam and βc the velocity.

The interaction further excites plasma electron density and electromagnetic surface waves propagating along the filament axis with comparable magnitude as the electron beam electric fields. They spread the beam-induced perturbation outward, beyond the direct beam field-excited region, up to the limits of the centimeter-long plasma column, and heat plasma electrons not directly affected by beam fields (see Supplemental Video 1 [35]).

Because of the attracting plasma ions, lower-energy plasma electrons expelled from the initial plasma volume perform complex oscillations around the filament, which evolve due to combined effects of initial kick, plasma density waves, and electromagnetic plasma fields. These oscillations are inherently anharmonic, because the nominal plasma wavelength $\lambda_p = 2\pi c/(n_e e^2/m_e \epsilon_0)^{1/2} \approx 77~\mu m$ is of the order of the initial plasma diameter. Thus, a large fraction of plasma electrons periodically propagates through the surrounding gas causing impact ionization, as they periodically exhibit instantaneous kinetic energies $W_{kin} > W_{thresh,H2} \approx 15.4$ eV and $W_{kin} > W_{thresh,He} \approx 24.6$ eV [33], at which impact ionization cross sections peak. Over time, this process accumulates substantial additional plasma. The spectral evolution of the plasma electrons is shown in Fig. 3 and Supplemental Video 2 [35]. On timescales far beyond the reach of PIC simulations, the complex plasma dynamics further cause ion motion and expand the initial volume substantially compared to the laser-only case, as evident from comparing Figs. 1(b) and 1(c). In summary, the seed plasma electrons' kinetic energy originating from rapid and confined energy transfer from the electron beam gradually creates additional plasma. Eventually, this additional plasma recombines, and associated relaxation processes produce the greatly amplified plasma afterglow signal observed by the CCD camera.

We apply these findings to measure spatial alignment and TOA between the electron beam and laser pulse. In both measurement modes, changing their geometric overlap varies the fraction of electron beam fields transferring energy into the plasma and, thus, the resulting afterglow amplification. The first mode scans spatial alignment with fixed relative TOA $\Delta t_{delay} = TOA_{laser} - TOA_{e-beam} \approx 2.1$ ps, such that a fully formed seed plasma is generated ahead of the electron beam arrival. By introducing a shift Δy between laser and electron beam, the electron beam fields intersect to a lesser degree with the seed plasma volume, which reduces energy transfer. Consequently, the integrated afterglow signal peaks for central overlap $\Delta y = 0$ and decreases with larger offsets $|\Delta y| > 0$. When increasing $|\Delta y|$, eventually the amplification ceases completely, yielding only the afterglow from the unperturbed filament. Figure 4 presents a Δy-alignment scan with Gaussian plasma afterglow distribution and width $\sigma_y = 64.8~\mu m$ (rms). This curve agrees well with the electron beam energy loss in PIC simulations obtained for varying spatial overlap with the plasma volume: The plasma
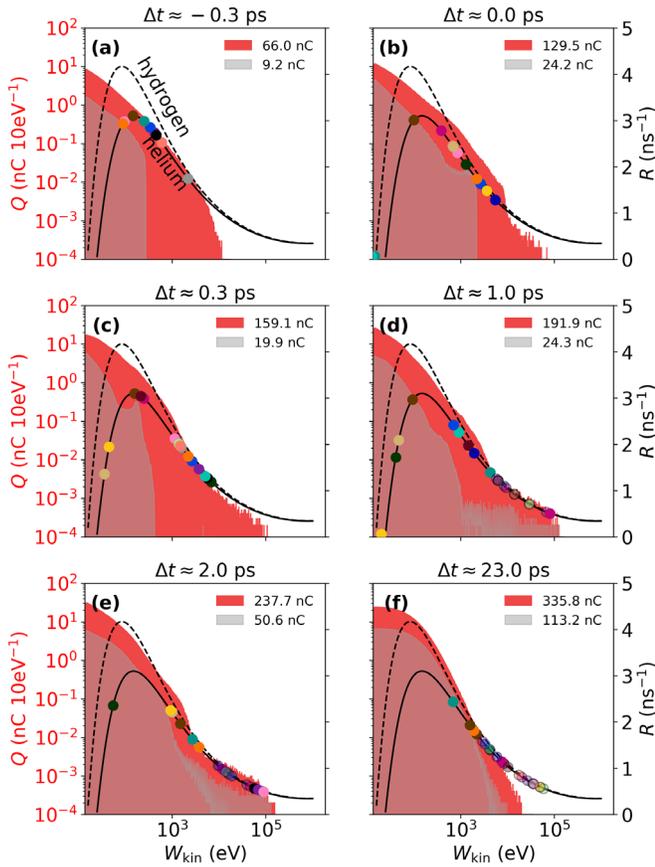
FIG. 3. Simulated evolution of the spectral plasma electron distribution Q ($W_{kin} > W_{thresh,H2} \approx 15.4$ eV) outside (red) and inside (gray) the seed plasma region with radius 24 μm. (a)–(e) During the initial interaction, the electron energies quickly assume a broadband, nonrelativistic distribution. (a)–(f) Colored circles represent oscillating electrons shown in Fig. 2 to indicate their changing energies and corresponding momentary cross sections σ_{Gas}. Electrons inside (transparent) the initial plasma volume cannot collide with neutrals, while electrons outside (solid) ionize ambient neutral gas at impact ionization rates $R = \sigma_{Gas} n_{Gas} \beta c$ per electron (black lines).
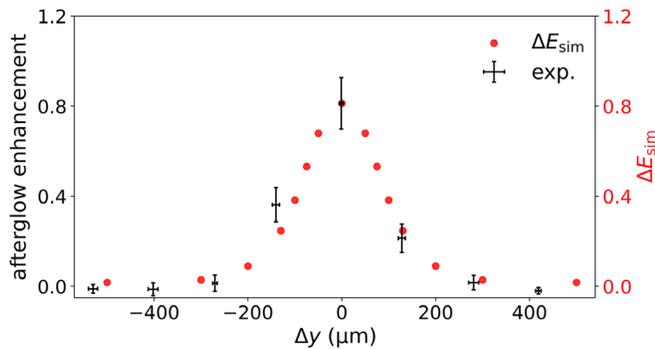
effectively samples the electron beam shape. We emphasize this apparently linear relation between the energy transferred into the plasma and the afterglow amplification because of the highly nonlinear dynamics discussed in the context of Figs. 2 and 3. Comparing experiment and simulation, the central peak position corresponds to optimal overlap of electron beam and plasma axes and, therefore, can readily be established within the accuracy of the imaging system. From fitting the 99 shots in the given dataset, this position can be determined within 4.1 μm accuracy, which is substantially smaller than the dimensions of the electron beam and seed plasma. This plasma afterglow response constitutes a multishot alignment diagnostic with accuracy dependent on the number of shots and shot-to-shot jitter. If, furthermore, the dependency shown in Fig. 4 is sufficiently well characterized from either experiment or theory, it represents a gauge curve, allowing for single-shot quantification of absolute alignment between the electron and laser beam.

In the second measurement mode, spatial translation is fixed to $\Delta y \approx 0$, and relative TOA is varied. Then, a delay scan with consecutive shots from -2.5 ps $< \Delta t_{delay} <$ 4.0 ps reveals a strong correlation between TOA and afterglow signal, as shown in Fig. 5. The afterglow signal drops sharply when the electron beam arrives at the same time or earlier than the laser pulse, because the seed plasma volume is not yet (fully) formed. As result, the scan yields a sigmoidal transition with width ~780 fs (FWHM) between zero and maximal afterglow amplification. This range isolates the temporal overlap region of the laser pulse and electron beam and can be found quickly with a broad sweep of a linear stage.

On the steep quasilinear transition region around temporal concomitance $\Delta t_{delay} \approx 0$, the evolving plasma again samples the electron beam distribution. The resulting afterglow signal then reacts most sensitively to small changes in TOA and, therefore, allows for determining

FIG. 4. Spatial alignment scan with 8–10 shots per setting with experimentally observed plasma afterglow enhancement (black) and normalized energy transfer obtained from simulation (red).
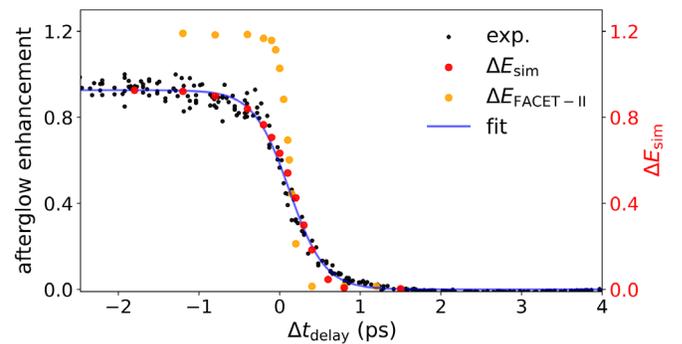
FIG. 5. Experimental time-of-arrival scan over 256 consecutive shots within -2.5 ps $< \Delta t_{delay} <$ 4.0 ps. Black: experimental normalized afterglow enhancement. Blue: sigmoid fit for experimental data. Red: normalized energy transferred into the plasma from PIC simulations. Orange: a FACET-II-class beam yields a substantially steeper transition.

the beam-laser synchronization with high resolution. We quantify this by calibrating the data with EOS time stamps with an accuracy of 25.8 fs to counteract the system-inherent shot-to-shot TOA jitter of ∼109 fs and by fitting the resulting curve with a sigmoid function $s(\Delta t_{\text{delay}}) = y_0 + a/(1 + e^{(\Delta t_{\text{delay}} - t_0)/k})$. The inverse function represents a TOA diagnostic based on the measured afterglow signal. Its accuracy, obtained from error propagation, assumes a minimal value of 26.7 fs at the turning point of the transition, which reflects the EOS time stamp accuracy. Artificially removing the uncertainty imposed by the EOS from the analysis yields ∼6.7 fs as the combined contribution from the experimental parameter jitter and the fit. We, therefore, expect significant potential for further improvement.

Again, there is good agreement between measurement and simulation, and the sigmoid shape obtained from PIC supports the linear relation between transferred energy and the measured afterglow amplification in the explored parameter regime. This relationship implies that the plasma effectively samples the beam envelope, allowing for precise determination of the TOA. Characterizing the "gauge curve" obtained, e.g., from simulations with sufficient precision can allow for single-shot TOA measurements, particularly when other sources of parameter jitter are low or measured independently.

The obtainable resolution of the technique depends on the dynamic range and photon collection efficiency of the experimental detector setup and the gradient of the respective transition. The corresponding shape is a function of the beam-plasma overlap, and its amplitude is given by the transferred energy. The latter is sensitive to multiple interaction parameters: electron beam duration and radius (see Supplemental Figs. S1 and S2 [35]) and charge [36]; laser pulse intensity and power; and gas density. For example, the simulated transition for shorter and narrower electron beams at FACET-II ($\sigma_z = 20 \ \mu$m, $\sigma_{x,y} = 10 \ \mu$m, $Q_b = 2.0$ nC, and $n_b/n_e = 0.1$) shown in Fig. 5 displays a 4 times steeper transition. The sensitivity and multiparameter dependency of the amplified plasma afterglow, hence, allows further optimized resolution and, additionally, enables a versatile diagnostic which can measure various parameters of the interaction.

On the other hand, the latter implies that the resolution of the quantity of interest is susceptible to the shot-to-shot jitter of other interaction parameters. Full exploitation of the versatility and sensitivity of this method, therefore, requires, as is true of many diagnostics, minimization of jitter contributions (a general goal of any facility) and/or their simultaneous measurement with auxiliary diagnostics. The latter can also be addressed by simultaneous composite measurements applied to the same shot, e.g., by exploiting multiple filaments in different measurement modes, which could isolate and deconvolve the parametric dependencies. At advanced stability and reduced shot-to-shot jitters as

attainable at modern photocathode-based facilities such as free-electron lasers, subfemtosecond and submicrometer resolution may be ultimately obtainable. In the measurements reported here, we exploited a single observable, namely, the time-integrated afterglow signal count of a single recombination line. By measuring the afterglow pattern spectrally, temporally, and spatially resolved, further information may be extracted in future developments of the scheme, which may improve the meaningfulness of the technique further.

We emphasize the applicability of the minimally invasive plasma afterglow amplification effect for intense and focused beams, as plasma-based techniques are not limited by conventional damage thresholds, its potential for measurements with ultrasmall footprint in the beam line and directly at the IP, and even in the presence of plasma. This capability was exploited to facilitate the first plasma photocathode injection experiment [17], which relies on precise spatiotemporal alignment and synchronization to release electrons inside a small fraction of an ∼100-μm-long plasma wave via tunneling ionization. The sensitivity of the afterglow amplification to various interaction parameters further offers capabilities for electron beam metrology. This opens numerous experimental opportunities, e.g., for pump-probe experiments, for the optimization of brilliant light sources, advanced and staged plasma accelerator schemes, and beam-laser experiments probing quantum electrodynamics.

---

[1] S. Schulz, I. Grguraš, C. Behrens, H. Bromberger, J. T. Costello, M. K. Czwalinna, M. Felber, M. C. Hoffmann, M. Ilchen, H. Y. Liu, T. Mazza, M. Meyer, S. Pfeiffer, P. Prędki, S. Schefer, C. Schmidt, U. Wegner, H. Schlarb, and A. L. Cavalieri, Femtosecond all-optical synchronization of an x-ray free-electron laser, Nat. Commun. 6, 5938 (2015).

[2] A. E. Gleason, C. A. Bolme, H. J. Lee, B. Nagler, E. Galtier, D. Milathianaki, J. Hawreliak, R. G. Kraus, J. H. Eggert, D. E. Fratanduono, and others, Ultrafast visualization of crystallization and grain growth in shock-compressed SiO2, Nat. Commun. **6,** 8191 (2015).

[3] F. Albert and A. G. R. Thomas, Applications of laser wakefield accelerator-based light sources, Plasma Phys. Controlled Fusion **58,** 103001 (2016).

[4] E. Ferrari *et al.*, Widely tunable two-colour seeded free-electron laser source for resonant-pump resonant-probe magnetic scattering, Nat. Commun. **7,** 10343 (2016).

[5] U. Frühling, M. Wieland, M. Gensch, T. Gebert, B. Schütte, R. Krikunova, R. Kalms, F. Budzyn, O. Grimm, J. Rossbach, E. Plönjes, and M. Drescher, Single-shot terahertz-field-driven x-ray streak camera, Nat. Photonics **3,** 523 (2009).

[6] P. Catravas, E. Esarey, and W. P. Leemans, Femtosecond x-rays from Thomson scattering using laser wakefield accelerators, Meas. Sci. Technol. **12,** 1828 (2001).

[7] David J. Gibson, Scott G. Anderson, Christopher P. J. Barty, Shawn M. Betts, Rex Booth, Winthrop J. Brown, John K. Crane, Robert R. Cross, David N. Fittinghoff, Fred V. Hartemann, Jaroslav Kuba, Gregory P. Le Sage, Dennis R. Slaughter, Aaron M. Tremaine, Alan J. Wootton, Edward P. Hartouni, Paul T. Springer, and James B. Rosenzweig, PLEIADES: A picosecond Compton scattering x-ray source for advanced backlighting and time-resolved material studies, Phys. Plasmas **11,** 2857 (2004).

[8] F. V. Hartemann, D. J. Gibson, W. J. Brown, A. Rousse, K. Ta Phuoc, V. Mallka, J. Faure, and A. Pukhov, Compton scattering x-ray sources driven by laser wakefield acceleration, Phys. Rev. Accel. Beams **10,** 011301 (2007).

[9] N. D. Powers, I. Ghebregziabher, G. Golovin, C. Liu, S. Chen, S. Banerjee, J. Zhang, and D. P. Umstadter, Quasi-monoenergetic and tunable x-rays from a laser-driven Compton light source, Nat. Photonics **8,** 28 (2014).

[10] K. Chouffani, F. Harmon, D. Wells, J. Jones, and G. Lancaster, Laser-Compton scattering as a tool for electron beam diagnostics, Laser Part. Beams **24,** 411 (2006).

[11] J. M. Krämer, A. Jochmann, M. Budde, M. Bussmann, J. P. Couperus, T. E. Cowan, A. Debus, A. Köhler, M. Kuntzsch, A. Laso García, U. Lehnert, P. Michel, R. Pausch, O. Zarini, U. Schramm, and A. Irman, Making spectral shape measurements in inverse Compton scattering a tool for advanced diagnostic applications, Sci. Rep. **8,** 1 (2018).

[12] D. P. Umstadter, Method and apparatus for generating and accelerating ultrashort electron pulses, U.S. patent No. US5789876A (1987).

[13] E. Esarey, R. Hubbard, W. Leemans, A. Ting, and P. Sprangle, Electron Injection into Plasma Wakefields by Colliding Laser Pulses, Phys. Rev. Lett. **79,** 2682 (1997).

[14] J. Faure, C. Rechatin, A. Norlin, A. Lifschitz, Y. Glinec, and V. Malka, Controlled injection and acceleration of electrons in plasma wakefields by colliding laser pulses, Nature (London) **444,** 737 (2006).

[15] B. Hidding, G. Pretzler, J. B. Rosenzweig, T. Königstein, D. Schiller, and D. L. Bruhwiler, Ultracold Electron Bunch Generation via Plasma Photocathode Emission and Acceleration in a Beam-Driven Plasma Blowout, Phys. Rev. Lett. **108,** 035001 (2012).

[16] F. Li, J. F. Hua, X. L. Xu, C. J. Zhang, L. X. Yan, Y. C. Du, W. H. Huang, H. B. Chen, C. X. Tang, W. Lu, C. Joshi, W. B. Mori, and Y. Q. Gu, Generating High-Brightness Electron Beams via Ionization Injection by Transverse Colliding Lasers in a Plasma-Wakefield Accelerator, Phys. Rev. Lett. **111,** 015003 (2013).

[17] A. Deng, O. S. Karger, T. Heinemann, A. Knetsch, P. Scherkl, G. G. Manahan, C. I. Clarke, S. Z. Green, C. A. Lindstrøm, E. Adli, R. Zgadzaj, M. C. Downer, G. Andonian, A. Murokh, D. L. Bruhwiler, J. R. Cary, M. J. Hogan, V. Yakimenko, J. B. Rosenzweig, and B. Hidding, Generation and acceleration of electron bunches from a plasma photocathode, Nat. Phys. **15,** 1156 (2019).

[18] X. Yan, A. M. MacLeod, W. A. Gillespie, G. M. H. Knippels, D. Oepts, A. F. G. Van Der Meer, and W. Seidel, Subpicosecond Electro-Optic Measurement of Relativistic Electron Pulses, Phys. Rev. Lett. **85,** 3404 (2000).

[19] A. L. Cavalieri *et al.*, Clocking femtosecond x rays, Phys. Rev. Accel. Beams **8,** 114801 (2005).

[20] A. Brachmann *et al.*, Femtosecond operation of the LCLS for user experiments, in *Proceedings of the International Particle Accelerator Conference, Kyoto, Japan* (ICR, Kyoto, 2010), p. 2287.

[21] A. Angelovski, M. Kuntzsch, M. K. Czwalinna, A. Penirschke, M. Hansli, C. Sydlo, V. Arsov, S. Hunziker, H. Schlarb, M. Gensch, V. Schlott, T. Weiland, and R. Jakoby, Evaluation of the cone-shaped pickup performance for low charge sub-10 fs arrival-time measurements at free electron laser facilities, Phys. Rev. Accel. Beams **18,** 012801 (2015).

[22] F. Tavella, N. Stojanovic, G. Geloni, and M. Gensch, Few-femtosecond timing at fourth-generation x-ray light sources, Nat. Photonics **5,** 162 (2011).

[23] M. Harmand, R. Coffee, M. R. Bionta, M. Chollet, D. French, D. Zhu, D. M. Fritz, H. T. Lemke, N. Medvedev, B. Ziaja, S. Toleikis, and M. Cammarata, Achieving few-femtosecond time-sorting at hard x-ray free-electron lasers, Nat. Photonics **7,** 215 (2013).

[24] A. L. Schmeltekopf and H. P. Broida, Short-duration visible afterglow in helium, J. Chem. Phys. **39,** 1261 (1963).

[25] D. R. Bates, Electron Recombination in Helium, Phys. Rev. **77,** 718 (1950).

[26] C. G. Durfee and H. M. Milchberg, Light Pipe for High Intensity Laser Pulses, Phys. Rev. Lett. **71,** 2409 (1993).

[27] A. E. Martirosyan, C. Altucci, A. Bruno, C. De Lisio, A. Porzio, and S. Solimeno, Time evolution of plasma afterglow produced by femtosecond laser pulses, J. Appl. Phys. **96,** 5450 (2004).

[28] R. J. Shalloo, C. Arran, L. Corner, J. Holloway, J. Jonnerby, R. Walczak, H. M. Milchberg, and S. M. Hooker, Hydrodynamic optical-field-ionized plasma channels, Phys. Rev. E **97,** 053203 (2018).

[29] M. J. Hogan, T. O. Raubenheimer, A. Seryi, P. Muggli, T. Katsouleas, C. Huang, W. Lu, W. An, K. A. Marsh, W. B. Mori, C. E. Clayton, C. Joshi, and others, Plasma wakefield acceleration experiments at FACET, New J. Phys. **12,** 055030 (2010).

[30] M. Reiser, *Theory and Design of Charged Particle Beams*, 2nd 2008 ed. (Wiley-VCH, Weinheim, 1994).

[31] B. L. Schram, F. J. De Heer, M. J. der Wiel, and J. Kistemaker, Ionization cross sections for electrons (0.6–20 keV) in noble and diatomic gases, Physica (Utrecht) **31**, 94 (1965).

[32] M. V. Ammosov, N. B. Delone, and V. P. Krainov, Tunnel ionization of complex atoms and atomic ions in electromagnetic field, Sov. Phys. JETP **64**, 1191 (1986).

[33] R. L. Kelly, Atomic and ionic spectrum lines below 2000 Angstroms: Hydrogen through krypton, J. Phys. Chem. Ref. Data **16**, 12 (1987).

[34] C. Nieter and J. R. Cary, VORPAL: A versatile plasma simulation code, J. Comput. Phys. **196**, 448 (2004).

[35] See Supplemental Material at http://link.aps.org/supplemental/10.1103/PhysRevAccelBeams.25.052803 for PIC-simulation movies of the beam-plasma interaction and additional electron beam parameter scans.

[36] J. B. Rosenzweig, N. Barov, M. C. Thompson, and R. B. Yoder, Energy loss of a high charge bunched electron beam in plasma: Simulations, scaling, and accelerating wakefields, Phys. Rev. Accel. Beams **7**, 061302 (2004).